Smart Structures and Systems, *Vol. 28, No. 1 (2021) 69-87*
https://doi.org/10.12989/sss.2021.28.1.069

Deep learning-based functional assessment of piezoelectric-based smart interface under various degradations

Thanh-Truong Nguyen [1,2a], Jeong-Tae Kim [3b], Quoc-Bao Ta [3c],
Duc-Duy Ho [2,4d], Thi Tuong Vy Phan [5,6e] and Thanh-Canh Huynh*[7,8]

[1] *Industrial Maintenance Training Center, Ho Chi Minh City University of Technology (HCMUT),*
268 Ly Thuong Kiet Street, District 10, Ho Chi Minh City 700000, Vietnam
[2] *Vietnam National University Ho Chi Minh City (VNU-HCM), Linh Trung Ward, Thu Duc District, Ho Chi Minh City 700000, Vietnam*
[3] *Department of Ocean Engineering, Pukyong National University, 45 Yongso-ro, Daeyeon 3-dong, Namgu, Busan 48513, Republic of Korea*
[4] *Faculty of Civil Engineering, Ho Chi Minh City University of Technology (HCMUT),*
268 Ly Thuong Kiet, District 10, Ho Chi Minh City 700000, Vietnam
[5] *Center for Advanced Chemistry, Institute of Research and Development, Duy Tan University, Da Nang 550000, Vietnam*
[6] *Faculty of Environmental and Chemical Engineering, Duy Tan University, Danang 550000, Vietnam*
[7] *Center for Construction, Mechanics and Materials, Institute of Research and Development, Duy Tan University, Danang 550000, Vietnam*
[8] *Faculty of Civil Engineering, Duy Tan University, Danang 550000, Vietnam*

(*Received May 22, 2020, Revised April 8, 2021, Accepted April 14, 2021*)

Abstract. The piezoelectric-based smart interface technique has shown promising prospects for electro-mechanical impedance (EMI)-based damage detection with various successful applications. During the process of EMI monitoring and damage identification, the operational functionality of the smart interface device is a major concern. In this study, common functional degradations that occurred in the smart interface are diagnosed using a deep learning-based method. Firstly, the effect of functional degradations on the EMI responses is analytically discussed. Secondly, a critical structural joint is selected as the test structure from which EM measurement using the smart interface is conducted. Thirdly, a numerical model corresponding to the experimental model is established and updated to reproduce the measured EMI responses. By using the updated numerical model, the EMI responses of the smart interface under the common functional degradations, such as the shear lag effect, the adhesive debonding, the sensor breakage, and the interface detaching, are simulated; then, the functional degradation-induced EMI changes are characterized. Finally, a convolutional neural network (CNN)-based functional assessment method is newly proposed for the smart interface. The CNN can automatically extract and directly learn optimal features from the raw EMI signals without preprocessing. The CNN is trained and tested using the datasets obtained from the updated numerical model. The obtained results show that the proposed method was successful to classify four types of common defects in the smart interface, even under the effect of noises.

Keywords: CNN; debonding; deep learning; degradation; diagnosis; electromechanical; impedance characteristics; impedance method; piezoelectric sensor; sensor fault; shear lag; smart interface

1. Introduction

Sensing elements (e.g., sensors, actuators, transducers) play a key role in a structural health monitoring (SHM) system. With an array of sensing devices, structural responses of a monitored system can be easily recorded over time and utilized for various SHM tasks, such as damage identification, the evaluation of structural performance, the control of construction process. However, during their service life, the sensing devices inevitably experience performance degradations (e.g., degraded quality or failures), which can result from overloading, severe environmental effects, and material deteriorations. Such performance degradations will cause observable changes in the measured structural responses, which could be misinterpreted as the effect of structural damage.

Damage detection using electromechanical impedance (EMI) signatures has been a commonly favoured SHM method (Park *et al.* 2001, Song *et al.* 2008, Nguyen and Kim 2012). Traditionally, the impedance-based SHM method utilizes PZT (Lead Zirconate Titanate) patches, which are surface-bonded directly to a host structure, to measure the EMI in the high-frequency range (Kim *et al.* 2019). Since the EMI responses contain local dynamics of the host structure, the structural damage can be diagnosed by observing the variation in the measured EMI signatures. However, the direct attachment of the PZT often leads to weak EMI responses and further causes difficulties in determining sensitive frequency bands for a damage

---

*Corresponding author, Ph.D.,
E-mail: huynhthanhcanh@duytan.edu.vn
[a] Ph.D.
[b] Professor
[c] Ph.D. Student
[d] Professor
[e] Ph.D.

ISSN: 1738-1584 (Print), 1738-1991 (Online)

detection task (Kim *et al*. 2010, Min *et al*. 2010, Huynh *et al*. 2019). For a given target structure, the effective frequency bands are often unknown and traditionally identified by the try-and-error method. This is mainly due to the dependence of the sensitive frequency bands on local dynamic characteristics of the target structure. Embeddable piezoelectric-based sensing devices have been developed for enhancing damage sensitivity of the EMI, such as smart aggregates for SHM of concrete structure (Song *et al*. 2008, Yan *et al*. 2009), smart washers for critical connection monitoring (Nguyen *et al*. 2011, Nguyen and Kim 2012), for smart coupons for corrosion monitoring (Li *et al*. 2019). However, to obtain damage-sensitive EMI signatures, those piezoelectric devices must be inserted in the monitored structures during the construction, causing challenges when applied to existing structures.

To deal with the above problems, mountable piezoelectric devices have been proposed (Huynh and Kim 2014, Ryu *et al*. 2019, Tawie *et al*. 2019). The idea was pioneered in the reference (Annamdas *et al*. 2009). In their work, a PZT patch was indirectly mounted to the host structure via an additional interface with the purpose of easy installation. The PZT-interface system was mounted to a host structure to monitor the EMI response. The idea was then improved by changing boundary conditions of the substrate structure to form a mountable piezoelectric-based smart interface (Huynh and Kim 2014). The smart interface can be attached to and removed from a host structure via two outside bonded sections. The middle section of the smart interface was designed to create strong EMI resonances in a desired effective frequency range, thus enabling the predetermination of the sensitive frequency bands of the EMI (Huynh and Kim 2017). The use of the smart interface concept has been recently reported. A slender smart interface for tension force monitoring of axially loaded members was designed in the reference (Ryu *et al*. 2019). A circular piezoelectric interface was developed to enhance the EMI for SHM of a fibre composite plate (Tawie *et al*. 2019).

As the EMI-based method has been a widely accepted SHM approach, the evaluation of the operational functionality of the piezoelectric-based smart interface has become an important issue for practical applications. For damage identification, the EMI signature of an unknown state is statistically compared with the baseline signature of the undamaged state. However, the baseline signature varies with not only the structural damage but also the functional degradations of the piezoelectric device. The performance of the smart interface can be degraded due to sensor defects (e.g., sensor breakage), poor bonding layer (e.g., debonding and shear lag phenomena), or damaged interface (e.g., detaching from the host structure). Those degradations would modify structural and piezoelectric properties of the smart interface, leading to certain changes in measured EMI responses, causing false detection of structural damages. Thus, a reliable method should be sought for the assessment of the functionality of the smart interface during SHM tasks.

In the past years, some researchers have put their efforts into assessing the operational conditions of PZT sensors for the impedance-based method. One of the first attempts was to estimate the effect of the degraded bonding layer on the EMI, as reported in the reference (Giurgiutiu *et al*. 2002). Their study proposed a sensor debonding identification method via tracking the appearance of the PZT's resonance. Park *et al*. investigated extensively the problem with the consideration of more degradation types in the piezoelectric sensors (Park *et al*. 2006). Ai *et al*. assessed the sensor conditions and distinguished the sensor faults from the structural damage by using the features of the real admittance (Ai *et al*. 2016). Very recently, the effect of sensor defects on the EMI of a smart interface has been experimentally investigated (Huynh *et al*. 2020). Their study showed that the sensor defects could be distinguished from the structural damage using the gradient of the imaginary admittance signatures. However, the study considers only sensor breakage and sensor debonding in the experiment due to difficulties in forming realistic defects in the smart interface. During its service life, a smart interface could also experience the interface fault (i.e., interface debonding) and the shear lag phenomenon.

So far, most of the studies on the sensor fault diagnosis have used hand-crafted EMI features such as the gradient of the imaginary admittance or the statistical damage indices (Park *et al*. 2006, Ai *et al*. 2016, Huynh *et al*. 2020). The hand-crafted feature extraction process is not only time-consuming but also prevents the impedance-based method from the real-time operation. Recently, the convolutional neural network (CNN) has successfully solved many problems of pattern recognition in the SHM field (Abdeljaber *et al*. 2018, Azimi and Pekcan 2020, Huynh 2021). One of the advanced features of the CNN is the combination of the feature extraction and damage classification tasks into a unique learning block (Abdeljaber *et al*. 2018), providing the CNN with an ability to autonomously take out and directly learn optimal features from the raw signals. This allows to reduce computational costs and also provides an enhanced classification performance.

In this study, a CNN-based method is newly developed to assess the health status of a smart interface during SHM. At first, a refined impedance model is adopted to analytically interpret the effect of the smart interface's degradations on the EMI response. Next, a critical girder connection is selected as a host structure to conduct real impedance measurement via the smart interface. Then, a finite element (FE) model corresponding to the experimental model is established and fine-tuned by a sensitivity-based algorithm. The numerical EMI responses are compared with the experimental ones to show the reliability of the updated FE model. Afterwards, common functional degradations of the smart interface, including the shear lag effect, the adhesive debonding, the sensor breakage, and the interface detaching, are modelled using the updated FE model; then, the functional degradation-induced EMI changes are analyzed. Lastly, a CNN-based functional assessment method is designed for the smart interface. Based on the EMI characterization, the imaginary part is selected as the input for the CNN. The output of the network includes the four classes of operational conditions

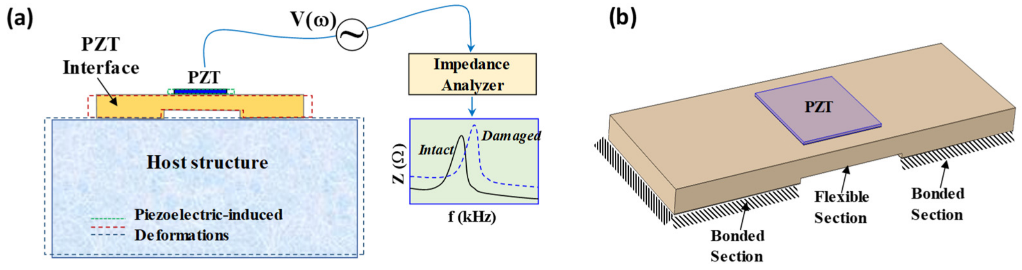

Fig. 1 (a) Overview of the piezoelectric interface-based impedance monitoring method; (b) Smart interface prototype

of the smart interface: "Healthy", "PZT-bond defect", "PZT-breakage", "Interface-debonding". The CNN is trained using the numerical EMI signals generated from the updated FE model and tested using the corresponding noise-contaminated signals. The obtained results show that the proposed method is of high accuracy with an overall precision of 99%.

The originality of this study and its contribution to the SHM community include: (1) a newly-developed deep learning-based method for functional assessment of a degraded smart interface is presented; (2) the developed method can directly process the raw EMI signal without preprocessing; therefore (3) the method is promising for real-time assessment of the functionality of the smart interface; and (4) this study is expected to provide a reliable diagnostic tool for the degraded smart interface during SHM in practice.

2. Impedance monitoring approach via smart interface

2.1 Piezoelectric-based smart interface

The overview of the piezoelectric-based smart interface technique is depicted in Fig. 1(a). The smart interface is a substructure embedded with a PZT patch. To acquire the EMI response, the PZT is excited by a harmonic voltage ($V(\omega)$) in the high-frequency domain via an impedance analyzer. Due to the inverse piezoelectric effect, the PZT is expanded and its deformation initiates the coupling between the interface and the host structure, which simultaneously results in an output current ($I(\omega)$) following the direct piezoelectric effect. The output current is recorded by the impedance analyzer and the EMI is obtained as $Z(\omega) = V(\omega)/I(\omega)$.

The smart interface prototype is shown in Fig. 1(b). The prototype is a plate-like structure and the PZT is surface-bonded at the middle. The smart interface can be easily bonded to the target structure via two outside sections. The middle of the interface is intentionally designed with a flexible section to enable an easy elongation of the PZT along with the piezoelectric effects, which consequently creates strong resonances in the measured EMI.

If the structural damage occurred in the host structure, the modal parameters of the coupled interface-host structure system will vary, causing alternations in the EMI of the system. In a typical way, structural damage is diagnosed by comparing the post- and after-damage EMI signatures using statistical damage metrics.

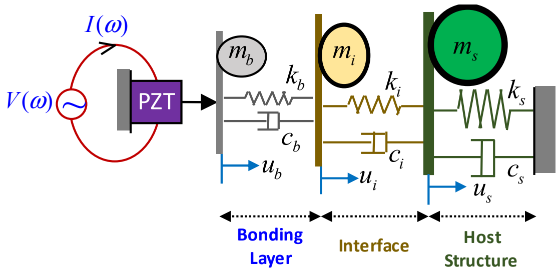

Fig. 2 Analytical refined impedance model

2.2 Electromechanical impedance model

Under the piezoelectric excitation, the system shown in Fig. 1(a) has coupling interactions between the sensor and the interface, between the interface and the host structure. To describe such interactions, a simplified impedance model of the interface-host structure system can be used (Huynh and Kim 2017). However, this model did not consider the role of the bonding layer in the EMI formulation, which can be used to describe the shear lag effect and the sensor debonding (Jin and Wang 2011, Bhalla and Moharana 2012).

In this study, a recently-developed impedance model was adopted to represent the effect of degradations in the smart interface (Huynh *et al*. 2020). As seen in Fig. 2, the refined impedance model is a 3-dof spring-mass-damper system, in which one dof refers to the host structure (m_s, k_s, c_s), and two remaining dofs refer to the interface (m_s, k_s, c_s) and the bonding layer (m_b, k_b, c_b), respectively. Once a harmonic voltage excitation $V(\omega)$ is applied to the PZT, a harmonic force f_b is introduced into the impedance model at the PZT driving point. The equation of motion of the 3-dof system under the external force f_b can be expressed in Eq. (1), in which $x_b, \dot{x}_b, \ddot{x}_b$; $x_i, \dot{x}_i, \ddot{x}_i$; $x_s, \dot{x}_s, \ddot{x}_s$ are the displacements, velocities, and accelerations corresponding to the masses m_b, m_i and m_s, respectively.

$$\begin{bmatrix} m_b & 0 & 0 \\ 0 & m_i & 0 \\ 0 & 0 & m_s \end{bmatrix} \begin{Bmatrix} \ddot{x}_b \\ \ddot{x}_i \\ \ddot{x}_s \end{Bmatrix} + \begin{bmatrix} c_b & -c_b & 0 \\ -c_b & c_b + c_i & -c_i \\ 0 & -c_i & c_i + c_s \end{bmatrix} \begin{Bmatrix} \dot{x}_b \\ \dot{x}_i \\ \dot{x}_s \end{Bmatrix} + \begin{bmatrix} k_b & -k_b & 0 \\ -k_b & k_b + k_i & -k_i \\ 0 & -k_i & k_i + k_s \end{bmatrix} \begin{Bmatrix} x_b \\ x_i \\ x_s \end{Bmatrix} = \begin{Bmatrix} f_b \\ 0 \\ 0 \end{Bmatrix} \quad (1)$$

Under the harmonic force $f_b = F_b e^{j\omega t}$, the steady-state displacements of the system can be defined as

$$x_b = X_b e^{j\omega t};\ x_i = X_i e^{j\omega t};\ x_s = X_s e^{j\omega t} \tag{2}$$

where X_b, X_i, and X_s are complex vibrational magnitudes of each dof, ω is the angular frequency, j is the unit imaginary number ($j^2 = -1$).

Substituting Eq. (2) into Eq. (1) will lead to an expression describing the coupled vibration responses of the whole system, as follows

$$\begin{bmatrix} -\omega^2 m_b + j\omega c_b + k_b & -j\omega c_b - k_b & 0 \\ -j\omega c_b - k_b & -\omega^2 m_i + j\omega(c_b + c_i) + (k_b + k_i) & -j\omega c_i - k_i \\ 0 & -j\omega c_i - k_i & -\omega^2 m_s + j\omega(c_i + c_s) + (k_i + k_s) \end{bmatrix} \begin{Bmatrix} X_b \\ X_i \\ X_s \end{Bmatrix} = \begin{Bmatrix} F_b \\ 0 \\ 0 \end{Bmatrix} \tag{3}$$

The mechanical impedance of the system $\bar{Z}$ (i.e., the bonding layer-interface-host structure system) is defined as the ratio between the excitation force f_b and the velocity $\dot{x}_b$ at the PZT driving point, as expressed in Eq. (4). The ratio F_b/X_b is easily determined by solving Eq. (3). By substituting F_b/X_b into Eq. (4), the mechanical impedance $\bar{Z}$ is expressed in Eq. (5), where the dynamic stiffness components K_{mn} (m, n = 1, 2, 3) are defined in Eq. (6).

$$\bar{Z} = \frac{f_b}{\dot{x}_b} = \frac{F_b}{j\omega X_b} \tag{4}$$

$$\bar{Z} = \frac{1}{j\omega}\left(K_{11} - \frac{K_{12}^2}{K_{11} + (K_{22} - \frac{K_{23}^2}{K_{33}})}\right) \tag{5}$$

$$\begin{gathered} K_{11} = -\omega^2 m_b + j\omega c_b + k_b;\ K_{12} = -j\omega c_b - k_b \\ K_{22} = -\omega^2 m_i + j\omega c_i + k_i;\ K_{23} = -j\omega c_i - k_i \\ K_{33} = -\omega^2 m_s + j\omega(c_i + c_s) + (k_i + k_s) \end{gathered} \tag{6}$$

The overall EMI Z is a combined function of the mechanical impedance of the system $\bar{Z}$ and that of the PZT sensor Z_a (Liang *et al*. 1994, Xu and Liu 2002), as follows

$$Z(\omega) = \left\{ j\omega C\left[1 - \frac{\bar{Z}}{\bar{Z} + Z_a}\frac{d_{31}^2 \hat{Y}_{11}^E}{\hat{\varepsilon}_{33}^T}\right]\right\}^{-1} \tag{7}$$

where $\frac{C=w_a l_a}{t_a \hat{\varepsilon}_{33}^T}$ is the capacitance of the PZT patch; $\hat{Y}_{11}^E = (1 + j\eta)Y_{11}^E$ is the complex Young's modulus of the PZT at the constant electric field; $\hat{\varepsilon}_{33}^T = \varepsilon_{33}^T(1 - j\delta)$ is the complex dielectric permittivity at the constant stress; d_{31} is the piezoelectric coupling constant at the zero stress; w_a, l_a, and t_a are respectively the effective width, length, and thickness of the PZT; η and δ are the structural damping loss factor and the dielectric loss factor of the PZT. The mechanical impedance of the PZT sensor, Z_a, is computed by $Z_a = \frac{\hat{Y}_{11}^E w_a t_a}{j\omega l_a}$.

The structural damage would modify the host structure's parameters (m_s, c_s, k_s), leading to the variation in the measured EMI responses, according to Eqs. (5)-(7). However, the EMI is also varied with degradations that occurred in the smart interface, which can result from overloading conditions, material deteriorations, and environmental changes.

2.3 Effect of functional degradations on EMI responses

By using the refined impedance model, imperfections in the bonding layer (e.g., debonding and shear lag phenomena), in the PZT sensor (e.g., sensor breakage/degraded quality), or in the interface structure (e.g., interface detaching) can be analyzed. Shear lag is a phenomenon of the difference in the PZT's strain relative to the interface's strain (Bhalla and Moharana 2012). When the stiffness of the bonding layer (k_b) is significantly reduced, the shear lag occurs, causing the reduction in the force and strain transmission between the PZT and the interface through the bonding layer. Thus, according to Eqs. (5-7), the shear lag effect certainly causes changes in the EMI through the bond stiffness (k_b).

When the PZT is debonded from the interface, the coupling between the PZT and the bonding layer is degraded (Park *et al.* 2008). As the result, the PZT debonding certainly causes a reduction in the piezoelectric coupling constant d_{31} of the PZT sensor, consequently leading to the change in the measured EMI responses, according to Eq. (7). In case of the sensor breakage/degradation, the effective sizes of the PZT patch are altered, leading to the changes in the capacitance C of the PZT, and thus modifying the measured EMI responses, following Eq. (7). If the interface is damaged, its structural parameters (m_i, c_i, k_i) would be changed. This will modify the dynamic stiffness components of the system, according to Eq. (6), resulting in the variations in the measured EMI response, following Eq. (7).

From the above analyses, it is analytically demonstrated that the shear lag phenomenon, the sensor breakage, the sensor debonding, and the interface's damage all will cause observable changes in the EMI signals. Those functional degradations should be timely detected using proper techniques to secure the reliability of the smart interface and to avoid false detection of structural damages during SHM.

3. Experimental and numerical investigations

The objective of this section is to establish a reliable testing model to simulate the degraded smart interface for analyzing the EMI characteristics and performing the functional assessment. Due to difficulties in creating realistic defects by the experiment, a predictable FE simulation strategy is adopted (Huynh 2020). The idea is to use an updated FE model to generate the reliable EMI response under various functional degradations in the smart

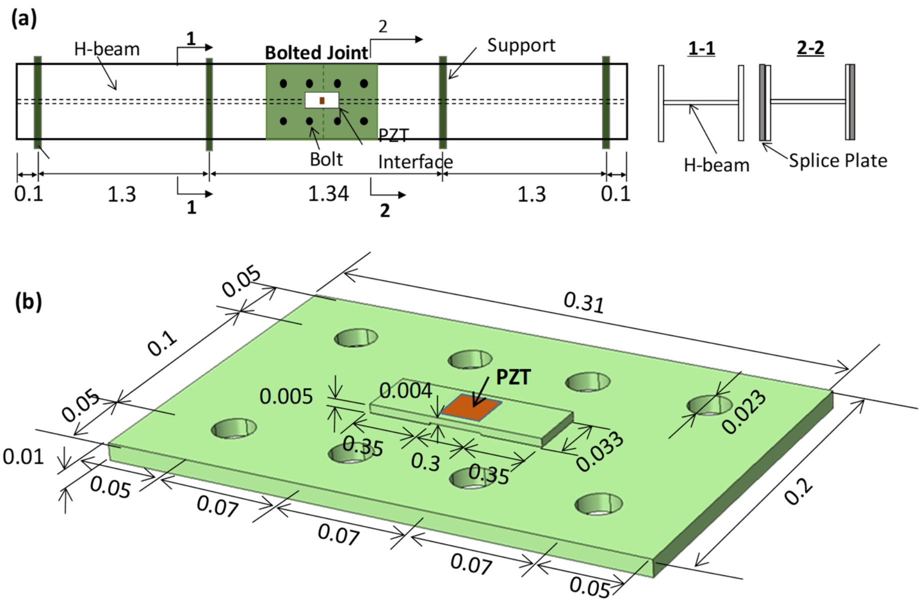

Fig. 3 Dimensional parameters of the testing model (a) Lab-scaled beam (b) Splice plate as the host structure

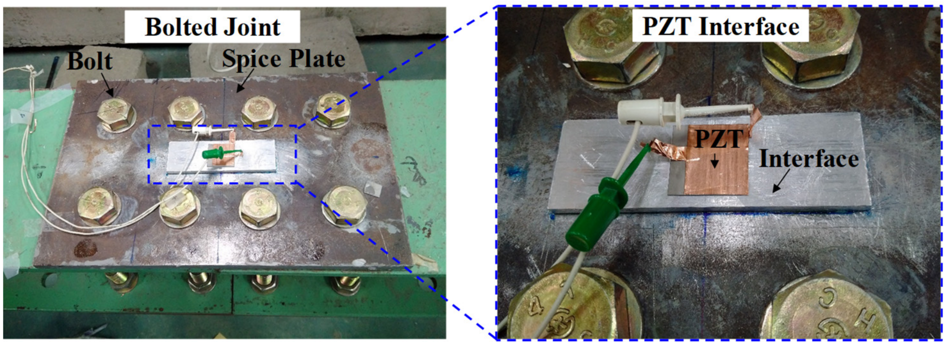

Fig. 4 Real view of the testing connection

interface. First, an experimental model is constructed and the impedance monitoring using the smart interface is carried out. Second, the FE model corresponding to the experimental model is established and the EMI response is numerically simulated. Last, the FE model is fine-tuned by a sensitivity-based model-updating algorithm. The reliability of the updated FE model is evidenced by reproducing the EMI signatures measured from the experiment.

3.1 Experimental investigation

The target structure is the bolted connection of a lab-scaled steel girder to conduct impedance measurement via the smart interface, as set up in Fig. 3(a). The target structure having a length of 3.96 m is assembled from two H-shaped girder segments through a bolted joint. The girder is simply supported via half-round steel rods. At the joint, the top and bottom flanges of the girder are clamped by a set of 16 bolts (Korean standard, 20 mm diameter) and two splice plates. All bolts are fastened by the same torque of 160 Nm.

The smart interface is fabricated from an aluminium plate and surface-mounted to the splice plate via two instant adhesive layers (Loctite 401). The geometric dimensions of the PZT-splice plate system are shown in Fig. 3(b). The two outside bonded sections of the interface have a thickness of 5 mm while the middle flexible section has a thinner thickness of 4 mm, see Fig. 3(b). The PZT patch (PZT-5A) is bonded to the flexible section via the instant adhesive layer (Loctite 401). Fig. 4 shows the real views of the bolted joint and the mounted PZT interface. It is noted that the experimental model in this study was adopted from the previous work (Huynh 2020).

A high-performance impedance analyzer, HIOKI 3532, was used to generate the harmonic excitation and recorded the EMI signatures from the smart interface. Particularly, the PZT was excited by a 1 V harmonic voltage in the frequency range of 10-55 kHz. During the impedance measurement, the room temperature was controlled at 21°C to avoid any effect caused by temperature changes.

The real and imaginary parts of the measured EMI responses are shown in Figs. 5(a) and (b), respectively (Huynh 2020). Two strong resonances of the EMI are seen in the frequency ranges of 15-18 kHz and 33-36 kHz. The

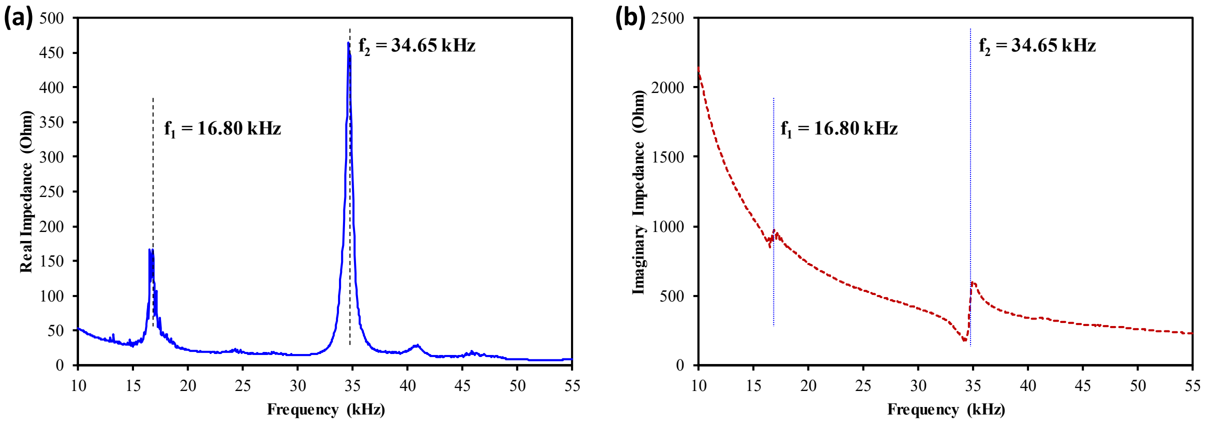

Fig. 5 Experimental EMI signatures (a) Real part; (b) Imaginary part

first resonant frequency (Peak 1) is 16.80 kHz ($f_{1,Exp}$) and the second resonant frequency (Peak 2) is 34.65 kHz ($f_{2,Exp}$). The resonant peaks correspond to the coupled vibrations of the smart interface-bolted connection system. The previous work proves that the contribution of the structural impedance to the overall EMI is significant at resonance (Nguyen and Kim 2012). Therefore, the resonant ranges of the EMI responses are often employed to maximize the damage detectability of the smart interface in practice.

3.2 Numerical investigation

3.2.1 Initial FE model

Piezoelectric effect simulation requires coupled electrical and mechanical responses, which occur simultaneously during the harmonic excitation of the PZT (Uddin *et al*. 2016, Mansoor *et al*. 2017, Dang *et al*. 2019). The previous FE model, which was well-established using COMSOL Multiphysics (Huynh, 2020) was adopted. The model consists of the PZT patch and its bonding layer, the interface body and its bonding layers, and the splice plate, as shown in Figs. 6(a) and (b). The dimensional parameters of the model are based on the actual geometry of the experimental model, see Fig. 3.

The model was meshed by 3D solid elements (2020 elements for the smart interface and the bonding layers, and 14118 elements for the splice plate), as seen in Fig. 6(a). Similar to the experiment, a 1V harmonic voltage was applied to the top surface of the PZT patch while the bottom was set as the ground electrode. The current generated due to the piezoelectric effects was measured during the PZT excitation. The EMI response was obtained as the ratio between the input voltage and the output current. Based on the previous studies (Johnson 1985, Ritdumrongkul *et al*. 2004), the experimental model was simplified by the smart interface-connection splice interacting system supported by a three-dimensional spring system (k_x, k_y and k_z) and a three-dimensional dashpot system (c_x, c_y and c_z), as shown in Fig. 6(a).

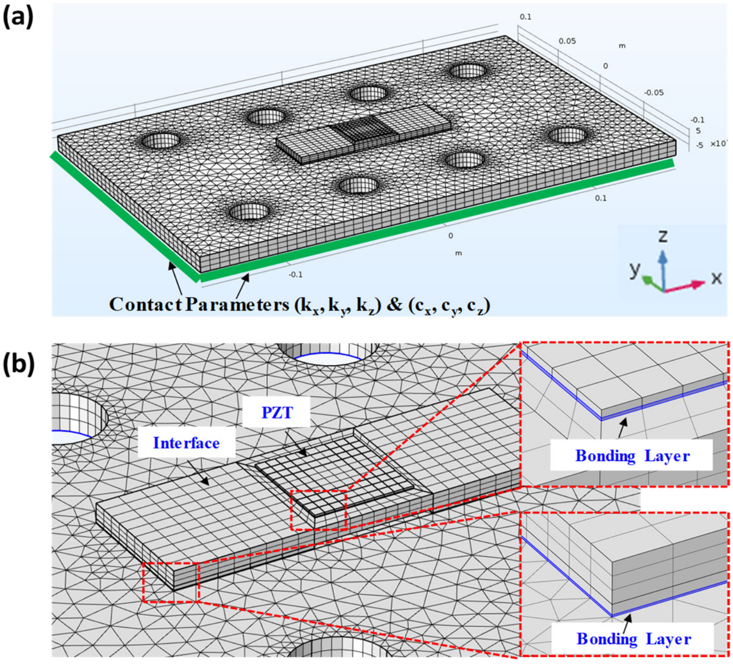

Fig. 6 FE modelling of the experimental model (a) Meshed model; (b) Smart interface and bonding layers

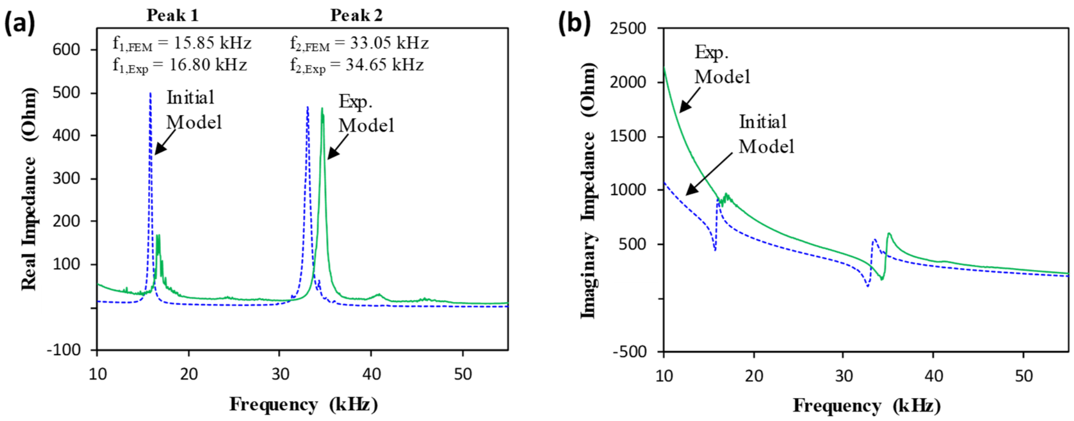

Fig. 7 EMI signatures of initial FE model vs experimental model (a) Real impedance; (b) Imaginary impedance

In the FE model, the splice plate was assigned by the steel material with Young's modulus E = 200 GPa, Poisson's ratio ν = 0.33, mass density ρ = 7850 kg/m^3. The interface body was assigned by the aluminum material with E = 70 Gpa, ν = 0.33, and ρ = 2700 kg/m^3. The PZT was assigned by the piezoelectric materials with the structural and piezoelectric properties obtained from the reference (Huynh *et al.* 2018). The z-directional contact stiffness was initially set as $k_z = 5.0 \times 10^{11}$ N/m^2/m and the x-directional and y-directional contact stiffness k_x and k_y were assumed to be 2.5×10^{11}. The dashpot system was represented by the damping ratios $\xi_x = \xi_y = \xi_z = 0.01$. From previously published data (Ong *et al.* 2003, Gresil *et al.* 2012), the bonding layers were first assumed to have the thickness t = 0.2 mm, Young's modulus E = 3 Gpa, Poisson's ratio ν = 0.38, and the mass density ρ = 1700 kg/m^3.

The EMI response of the initial FE model was analyzed in the frequency range of 10-55 kHz. The numerical EM signatures obtained from the initial FE model were compared with the ones measured from the experimental test, as shown in Fig. 7. Similar to the experiment, the FE simulation showed two remarkable resonant peaks in the real impedance signature of 10-55 kHz (see Fig. 7(a)). The frequencies of Peak 1 and Peak 2 were found at 15.85 kHz ($f_{1,\,FEM}$) and 33.05 kHz ($f_{2,\,FEM}$), respectively.

However, the FE model predicted the frequencies of Peak 1 and Peak 2 different from the experimental model (see Fig. 7(a)). The differences are also found in the imaginary impedance signatures (see Fig. 7(b)). To regenerate the experimental impedance signatures at the same frequency ranges with identical patterns, the structural parameters of the FE model should be fine-tuned by model-updating algorithms.

3.2 Updating FE model

3.3.1 Sensitive-based model-updating algorithm

The purpose of model-updating is to adjust a numerical model corresponding to a realistic model (Sirca and Adeli 2012). Through adjusting the structural parameters, the FE model can reproduce the measured EMI responses. In this work, the modal sensitivity-based system identification method, which is regarded as one of the reliable model-updating approaches (Shih *et al.* 2009, Pasquier and Smith 2016), was adopted to update the FE model.

The details of the modal sensitivity-based model-updating can be found in the previous study (Stubbs and Kim 1996). Herein, we only summarize the key steps. The first step is to determine the model-updating parameters of the FE model and measure the peak frequencies of the smart interface. The second step is to calculate the modal sensitivity of the model-updating parameters using the initial FE model. The third step is to compute the fractional changes in these parameters by the modal sensitivity equation. The final step is to repeat the whole process until the differences in the peak frequencies between the FE model and the experimental model are minimal.

3.3.2 Model-updating parameters

To secure the success of the model-updating process, proper structural parameters of the FE model should be properly selected. The rule is to select the unknown structural parameters and the structural parameters showing high sensitivities to the peak frequencies. Structural steel, aluminium alloy and PZT-5A are well-known materials and therefore the standard values are used. In the testing model, the structural parameters of the bonding layers are unknown and relatively uncertain. The Poison's ratio and the mass density of the bonding layer are approximate 0.38 and 1700 kg/m^3 with minor deviations while Young's modulus and the bond thickness have considerable deviations (Ong *et al.* 2003, Gresil *et al.* 2012). Young's modulus of the bonding layer has significant impacts on the high-frequency response of PZT sensors (Bhalla and Moharana 2012). Besides, the contact stiffness k_x, k_y and k_z are also unknown and depends on the bolt preload. The values of k_x and k_y were found to be around half of k_z (Huynh and Kim 2017), therefore k_x and k_y were set as $0.5 \times k_z$ during the model-updating process to reduce the number of unknown parameters. In summary, the bond thickness t_b, the bond Young's modulus E_b, and the contact stiffness k_z are selected as the model-updating parameters.

3.3.3 Updated FE model

Fig. 8 shows the modal sensitivities of the three model-updating parameters to the two identified frequencies of the impedance peaks (f_1 and f_2). It is shown that the bond thickness was the most sensitive to the frequency of Peak 1

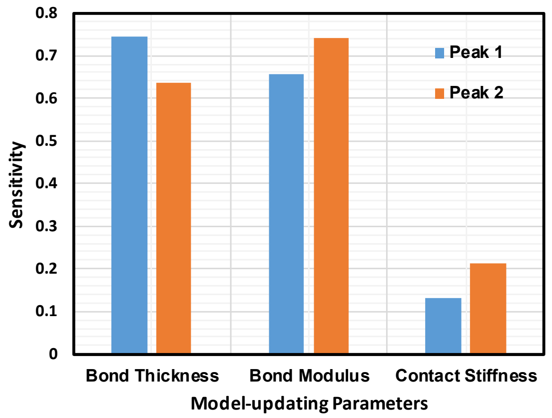

Fig. 8 Modal sensitivities of model-updating parameters

while the bond elastic modulus was the most sensitive to the frequency of Peak 2.

Next, the FE model was fine-tuned by the modal sensitivity-based algorithm. The experimental frequencies corresponding to the two impedance peaks were used as the target frequencies. Fig. 9 showed the convergence of the two peak frequencies of the FE model for the 27 iterations. In the beginning, the frequency error between the initial FE model and the experimental model was about 6% for Peak 1 and about 5% for Peak 2; however, the error was decreased to 0.3% for Peak 1 and 1.3% for Peak 2 at the 27th iteration. The FE model was converged with an average error of less than 1%.

The real part of the numerical EMI was compared with the experimental result in Fig. 11(a). Despite certain

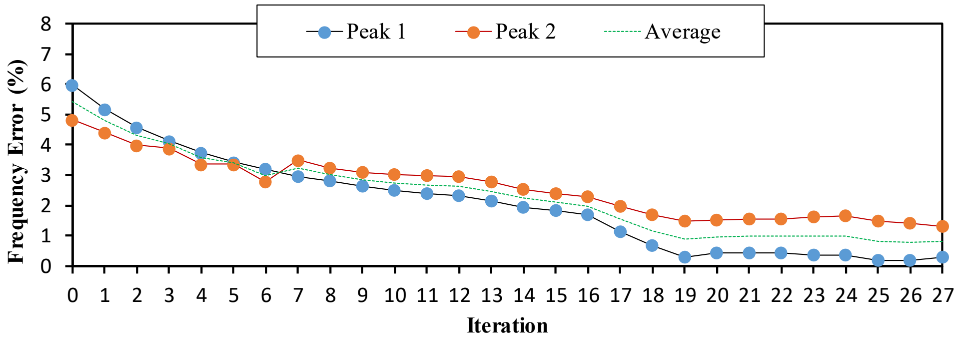

Fig. 9 Convergences of the two peak frequencies of the FE model

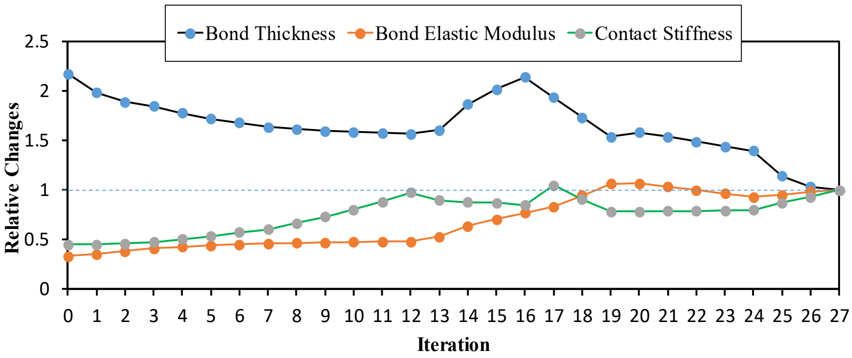

Fig. 10 Relative changes in the three model-updating parameters of the FE model

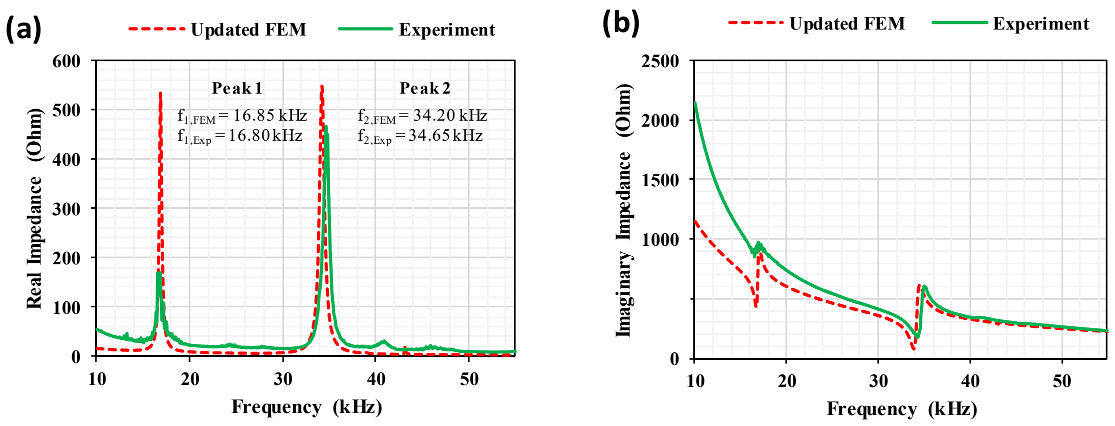

Fig. 11 EMI signatures of updated FE model (a) Real part; (b) Imaginary part

differences in the peak magnitude, it is obvious that the peak frequencies of the FE model were consistent with those of the experimental model at the identical frequency range with similar patterns. The consistency between the two models was also observed in the imaginary part of the EMI, see Fig. 11(b). Conclusively, the updated FE model reproduced the experimental EMI signatures. Thus, the fine-tuned FE model is feasible to estimate the EMI signatures of the smart interface under functional degradations.

As the numerical peak frequencies ($f_{1,FEM}$ and $f_{2,FEM}$) matched with the experimental ones ($f_{1,Exp}$ and $f_{2,Exp}$), the model-updating parameters are determined. Fig. 10 shows the relative changes in the three model-updating parameters, which are divided by the parameters at the 27th iteration. The figure shows that the parameters were converged to the unity at the final iteration.

4. Effect of functional degradations on EMI characteristics of smart interface

4.1 Simulation of common defects in smart interface and structural damage in host structure

The updated FE model was utilized to investigate the functional degradation-induced EMI characteristics of the smart interface. Potential degradations in the smart interface (i.e., shear lag effect, sensor debonding, sensor breakage, interface detaching) and structural damage (i.e., reduced Young's modulus of the spice plate) were numerically simulated. Then, EMI signatures were obtained from those FE simulations. Afterwards, the effects of the functional degradations and structural damage on the EMI and impedance features (i.e., the peak frequency and peak magnitude) were analyzed.

Firstly, the shear lag phenomenon was simulated by reducing the elastic modulus of the bonding layer (E_b). We simulated nine cases of the bond elastic modulus, as follows: $1 \times E_b$ (healthy), $0.5 \times E_b$, $0.1 \times E_b$, $0.05 \times E_b$, $0.03 \times E_b$, $0.02 \times E_b$, $0.005 \times E_b$, $0.001 \times E_b$, and $0.0001 \times E_b$.

Secondly, to simulate the sensor debonding effect, the size of the bonding layer was reduced in the horizontal and/or vertical directions, as described in Fig. 12(a). In the intact state, the bonding layer was filled over the bottom surface of the PZT. Then, six sensor debonding cases were modelled, including the cases of vertical debonding V1 (10%) and V2 (20%), horizontal debonding H1 (10%) and H2 (20%), and combined vertical and horizontal debonding V1H1 (19%) and V2H2 (36%).

Thirdly, to simulate the sensor breakage, the size of the PZT was reduced in the horizontal and/or vertical directions, as described in Fig. 12(b). In the intact state, the size of the PZT is the same as the size of the bonding layer. Six sensor breakage cases were simulated, including the cases of vertical breakage V1 (10%) and V2 (20%), horizontal breakage H1 (10%) and H2 (20%), and combined vertical and horizontal breakage V1H1 (19%) and V2H2 (36%).

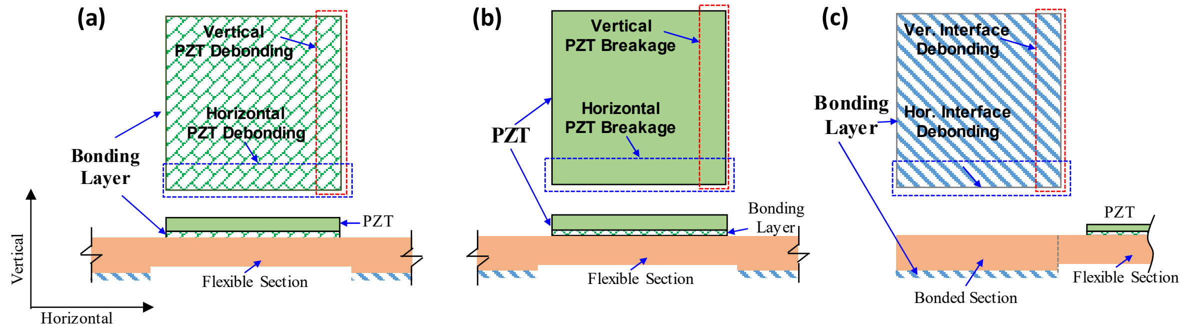

Fig. 12 Simulation of degraded PZT interface (a) PZT debonding; (b) PZT breakage; (c) Interface debonding

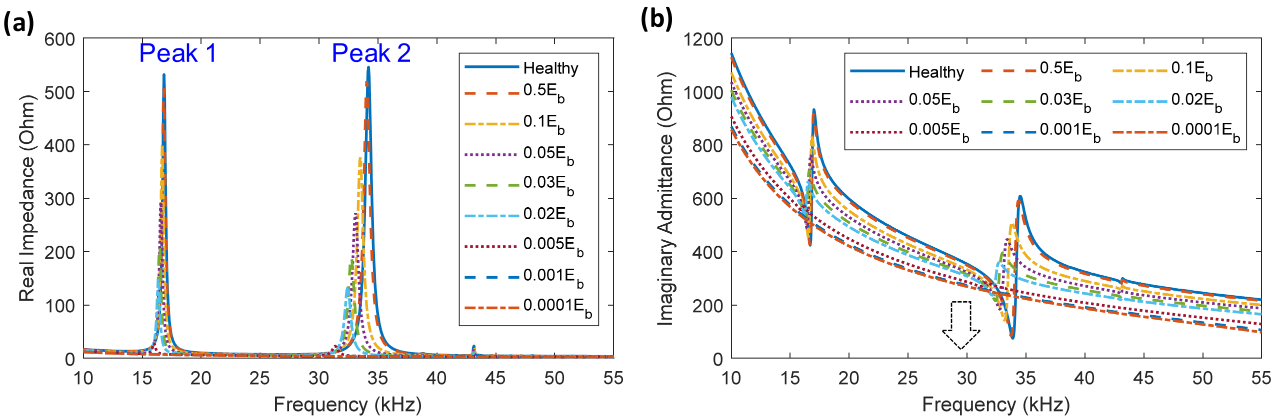

Fig. 13 Numerical EMI signatures under the shear lag effect (a) Real impedance; (b) Imaginary impedance

Fourthly, to simulate the phenomenon of interface detaching from the host structure (i.e., the splice plate), the adhesive layer of the interface was removed. Supposing that the interface was detached at the left bonded section. As shown in Fig. 12(c), in the intact state, the interface was completely attached to the host structure. Six interface detaching cases were modelled, including two vertical detaching V1 (23%) and V2 (46%), two horizontal detaching H1 (20%) and H2 (40%), and two combined vertical and horizontal detaching V1H1 (38%) and V2H2 (67%).

Finally, to simulate the structural damage, the elastic modulus of the splice plate E_{splice} (i.e., the host structure) was reduced in the FE model. Four cases of the elastic modulus: $1 \times E_{splice}$ (healthy), $0.8 \times E_{splice}$, $0.6 \times E_{splice}$, $0.4 \times E_{splice}$ were simulated.

4.2 Shear lag-induced EMI characteristics

Fig. 13(a) shows the real part of the EMI signatures for different values of the bond elastic modulus. The real EMI significantly varied with the bond stiffness. The signature of the imaginary part shifted down along with an increase of shear lag effect (i.e., a decrease of the bond stiffness), as seen in Fig. 13(b). Specifically, the real impedance peaks shifted down and left according to the shear lag effect. For the bond stiffness below $0.005E_b$, two impedance peaks were disappeared.

As key impedance features, the frequency and the magnitude of Peak 1 and Peak 2 were quantified under the shear lag effect. As respectively shown in Figs. 14(a) and (b), the magnitude and the frequency of the two peaks were reduced with a decrease of the bond stiffness. When the bond elastic modulus was reduced from $1 \times E_b$ to $0.005 \times E_b$, the two peak frequencies experienced similar reductions of about 500 Ω (see Fig. 14(a)) while the two peak magnitudes showed different variations: 0.85 kHz for Peak 1 and 2.85 kHz for Peak 2 (see Fig. 14(b)). The reduction rate of the 2nd frequency was faster than that of the 1st frequency, suggesting a larger impact of the shear lag effect on Peak 2.

4.3 Sensor debonding-induced EMI characteristics

The real and imaginary parts of the EMI were simulated for the six debonding cases of the PZT, as shown in Figs. 15(a) and (b). the sensor debonding caused obvious changes in the EMI responses. Interestingly, several new peaks appeared in the frequency ranges of 19-21 kHz and 37-44 kHz, which were resulted from the asymmetric piezoelectric force transmission from the debonded PZT to the interface. Similar to the shear lag effect, the sensor debonding caused

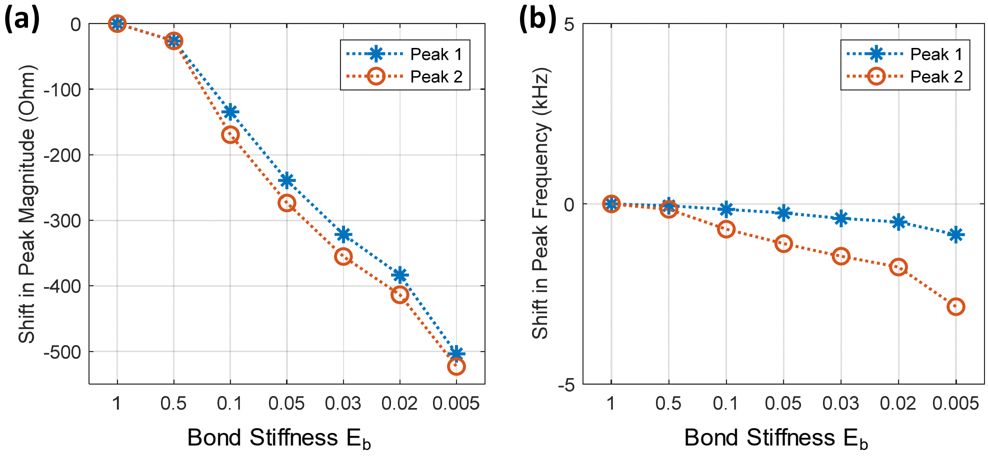

Fig. 14 Shifts in (a) Peak magnitude; and (b) Peak frequency due to the shear lag effect

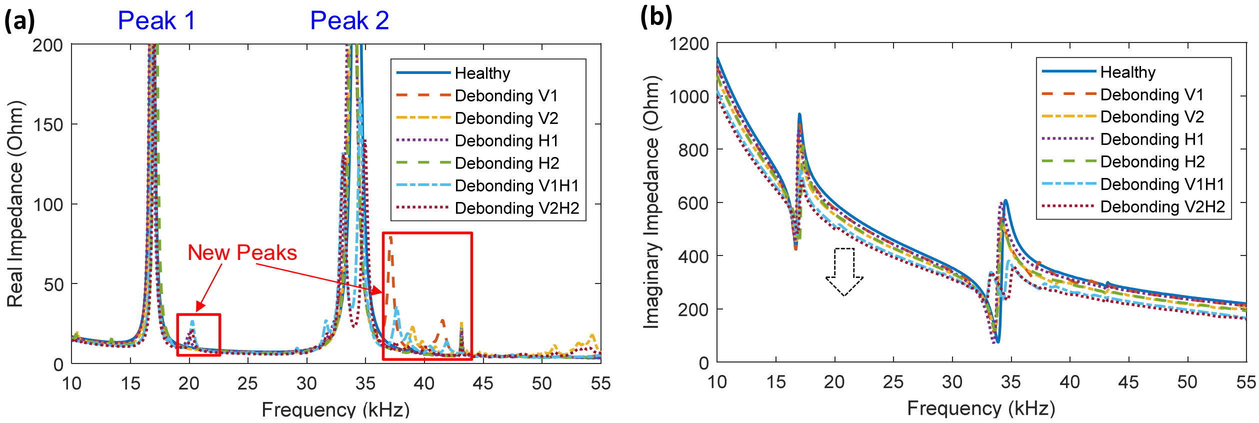

Fig. 15 Numerical EMI signatures under sensor debonding (a) Real impedance; (b) Imaginary impedance

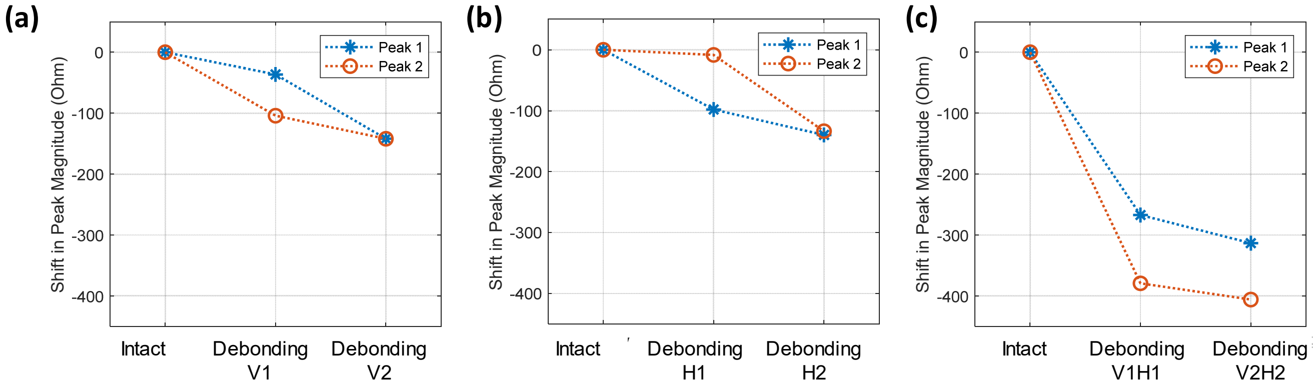

Fig. 16 Shifts in peak magnitudes due to sensor debonding (a) V1 & V2; (b) H1 & H2; (c) V1H1 & V2H2

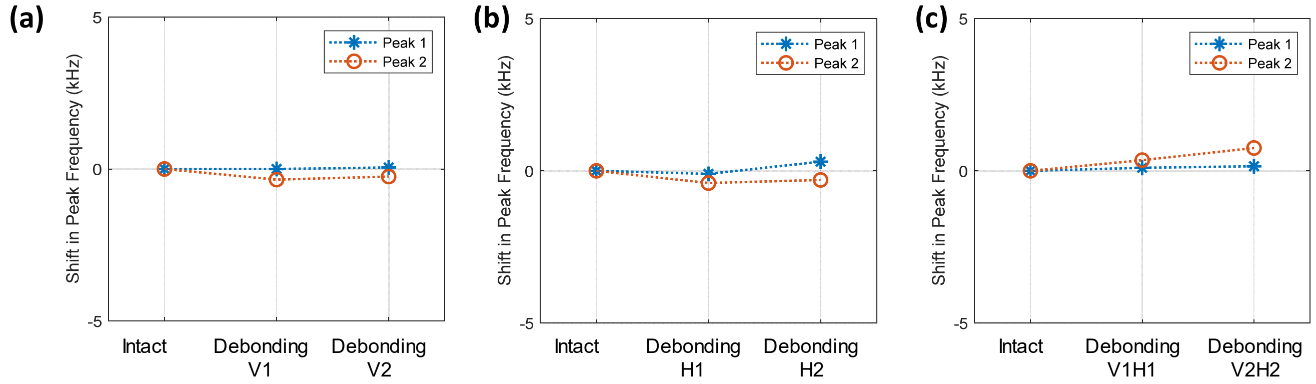

Fig. 17 Shifts in peak frequencies due to sensor debonding (a) V1 & V2; (b) H1 & H2; (c) V1H1 & V2H2

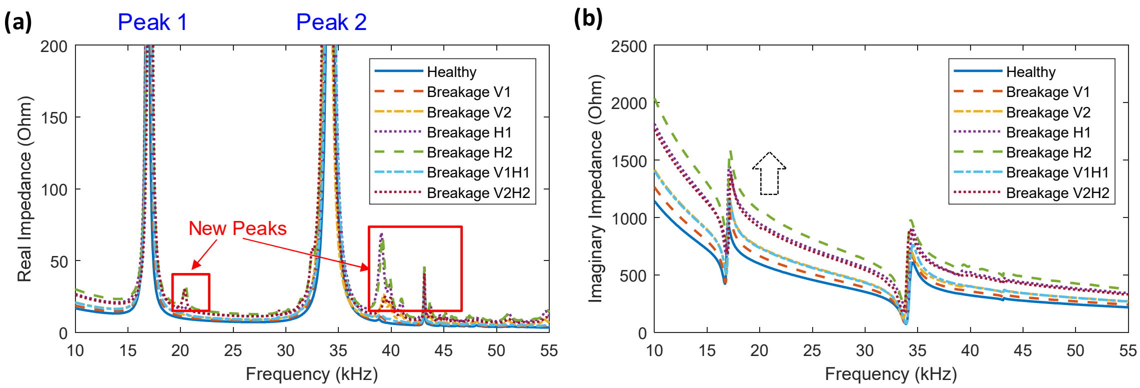

Fig. 18 Numerical EMI signatures under sensor breakage (a) Real impedance; (b) Imaginary impedance

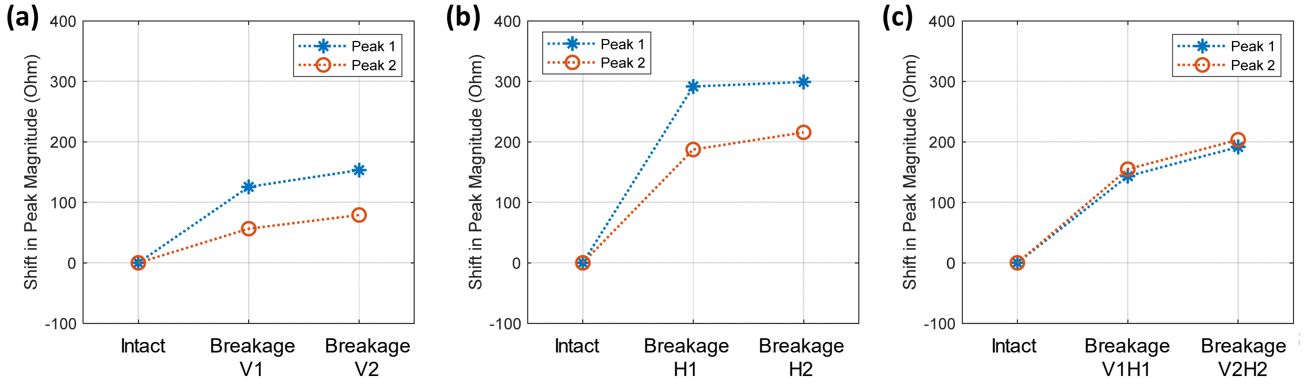

Fig. 19 Shifts in peak magnitudes due to sensor breakage (a) V1 & V2; (b) H1 & H2; (c) V1H1 & V2H2

downshifts in the imaginary EM signatures, see Fig. 15(b). The changes in the magnitude of Peak 1 and Peak 2 were quantified concerning the debonding direction of the PZT, as shown in Figs. 16(a), (b), and (c). Similar to the shear lag effect, the peak magnitude was decreased with an increase in the debonding severity. Two impedance peaks experienced relatively different changes in the peak magnitude (max variations: 310 Ω for Peak 1 and 405 Ω for Peak 2). Due to the higher debonding severity, the combined debonding cases (V1H1 and V2H2) showed higher changes in the peak magnitude as compared to others (V1, V2, and H1, H2).

The variation in the peak frequency was also computed for the intact and the six sensor debonding cases, as plotted in Fig. 17. It is observed that the sensor debonding caused slight changes in the peak frequencies (max variations: 0.3 kHz for Peak 1 and 0.75 kHz for Peak 2). The trend of the peak frequency variation was not apparent for the single direction of the debonding (V1, V2, and H1, H2). For the combined directions of the debonding (V1H1 and V2H2), the peak frequency was increased along with the debonding severity; specifically, the frequency change of Peak 2 was higher than that of Peak 1.

4.4 Sensor breakage-induced EMI characteristics

The real and imaginary parts of the obtained EMI responses were plotted in Figs. 18(a) and (b), respectively. The figures showed that the sensor breakage caused clear variations in the EMI signatures. As seen in Fig. 18(a), several additional peaks appeared in the frequency ranges of 19-21 kHz and 37-44 kHz. In contrast with the shear lag

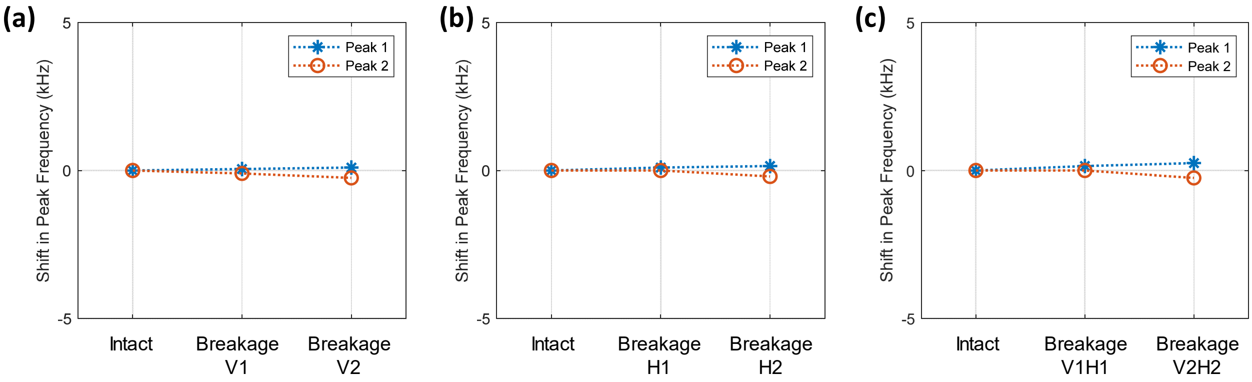

Fig. 20 Shifts in peak frequencies due to sensor breakage (a) V1 & V2; (b) H1 & H2; (c) V1H1 & V2H2

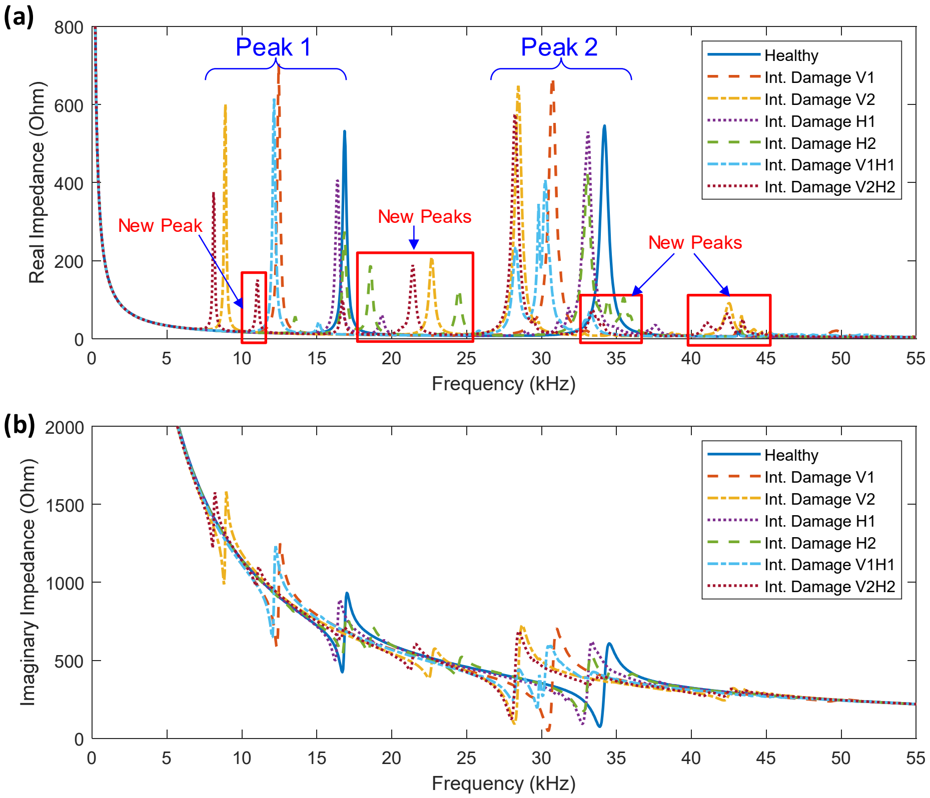

Fig. 21 Numerical EMI signatures under interface debonding (a) Real impedance; (b) Imaginary impedance

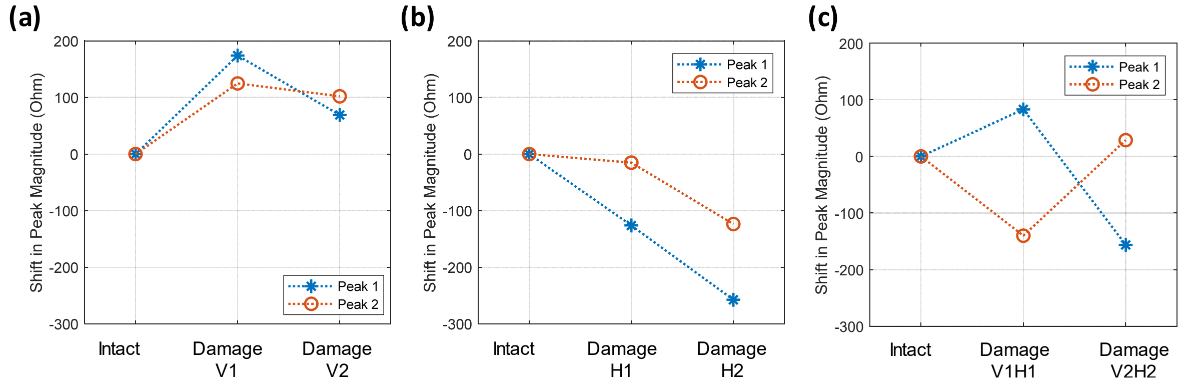

Fig. 22 Shifts in peak magnitudes due to interface detaching (a) V1 & V2; (b) H1 & H2; (c) V1H1 & V2H2

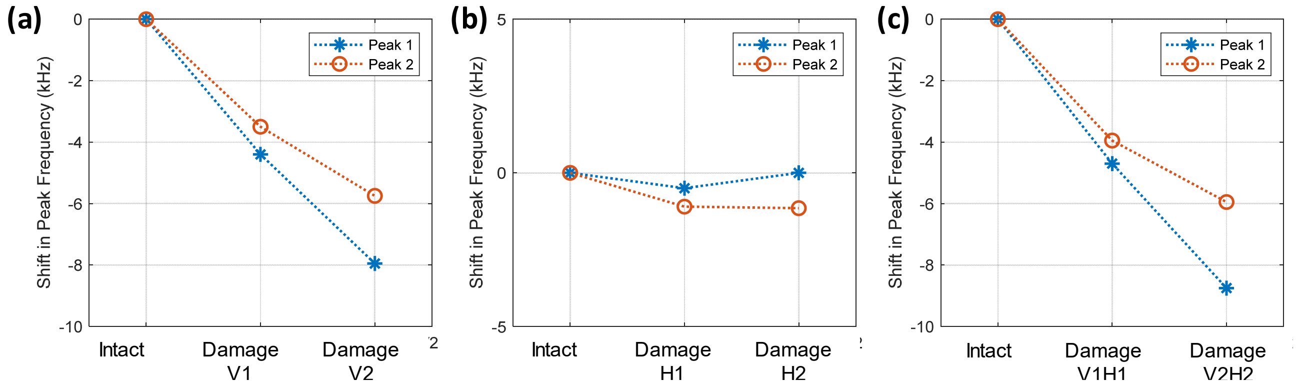

Fig. 23 Shifts in peak frequencies due to interface detaching (a) V1 & V2; (b) H1 & H2; (c) V1H1 & V2H2

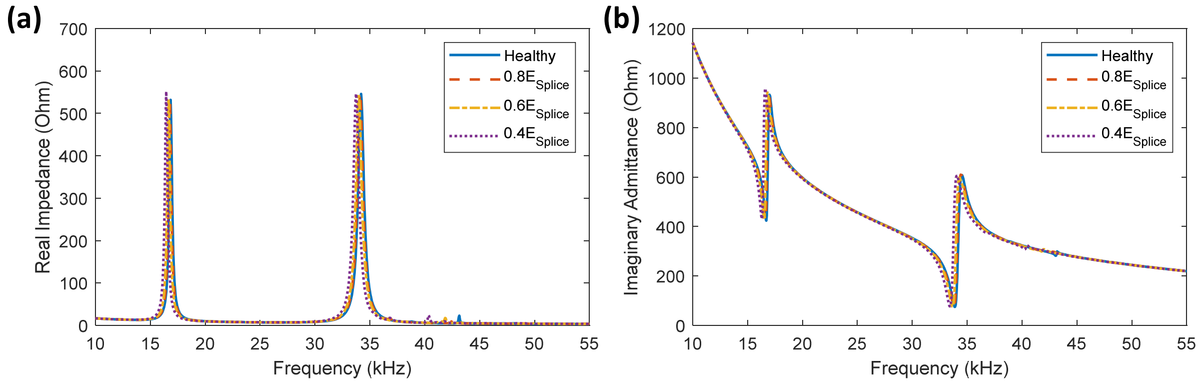

Fig. 24 Numerical EMI signatures under structural damage (a) Real impedance; (b) Imaginary impedance

and the sensor debonding phenomena, the breakage of the PZT caused upward shifts in the imaginary part of the EMI signatures, see Fig. 18(b).

The changes in the magnitudes of Peak 1 and Peak 2 were quantified concerning the breakage direction of the PZT, as shown in Fig. 19. In contrast with the adhesive layer's defects, the peak magnitude was increased with an increased debonding severity due to the sensor breakage. Two impedance peaks experienced relatively different changes in the peak magnitude (max variations: 300 Ω for Peak 1 and 205 Ω for Peak 2). The horizontal breakage cases (H1 and H2) caused higher changes in the peak magnitude as compared to others.

The frequency changes in Peak 1 and Peak 2 were computed accordingly. As observed in Fig. 20, the sensor breakage resulted in minor changes in the two peak frequencies (max variations: 0.25 kHz for Peak 1 and Peak 2). The frequency of Peak 1 was slightly increased with the breakage size of the PZT while that of Peak 2 was slightly decreased.

4.5 Interface detaching-induced EMI characteristics

Fig. 21(a) showed the real part of the EMI responses under the six detaching cases of the interface. It was observed that the interface detaching caused significant

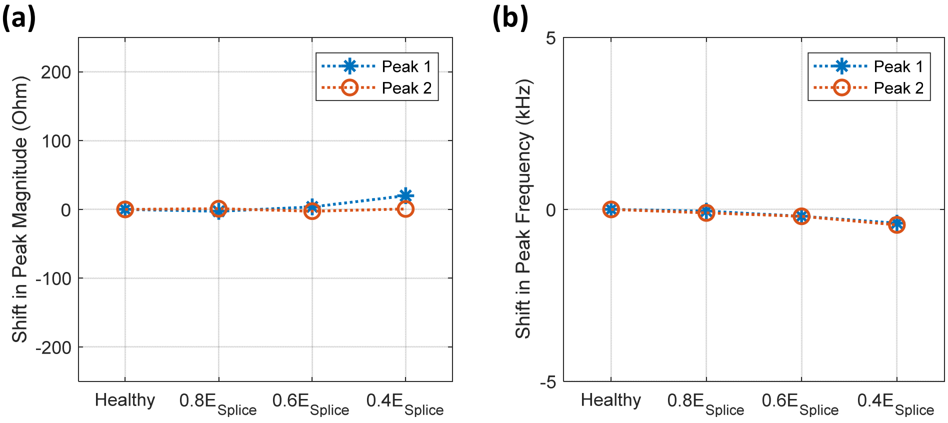

Fig. 25 Shifts in (a) Peak magnitude; and (b) Peak frequency due to structural damage

shifts in the two impedance peaks. Interestingly, many new peaks appeared in the frequency ranges of 10.5-11.5 kHz, 18-26 kHz and 34-45 kHz. The significant variations of the impedance peaks were also observed in the imaginary part of the EMI signatures, as plotted in Fig. 21(b). It was found that the interface detaching did not modify the overall curve of the imaginary part.

The changes in the peak magnitudes were quantified with regards to the detaching direction of the bonded section, including the vertical detaching cases: V1 and V2 (see Fig. 22(a)), the horizontal detaching cases: H1 and H2 (see Fig. 22(b)), and the combined detaching cases: V1H1 and V2H2 (see Fig. 22(c)). The peak magnitudes experienced significant changes (max variations: 260 Ω for Peak 1 and 140 Ω for Peak 2) under the effect of interface detaching; however, no apparent trend can be observed. The frequency changes in Peak 1 and Peak 2 were computed accordingly. As shown in Fig. 23(a), the vertical detaching cases V1 and V2 caused significant reductions in the peak frequencies; the frequency shift of Peak 1 was higher than that of Peak 2 (max variations: 8 kHz for Peak 1 and 5.75 kHz for Peak 2). As seen in Fig. 23(b), the horizontal detaching cases H1 and H2 caused less severe changes in the peak frequencies; the horizontal detaching majorly affected the frequency of Peak 2 (max variations: 0.5 kHz for Peak 1 vs 1.15 kHz for Peak 2). As observed in Fig. 23(c), the combined detaching cases V1H1 and V2H2 induced large variations in the two peak frequencies; the frequency shift of Peak 1 was higher than that of Peak 2 (max variations: 8.75 kHz for Peak 1 and 5.95 kHz for Peak 2).

4.6 Structural damage-induced EMI characteristics

Fig. 24(a) shows the real EMI signatures for different values of the elastic modulus. The EMI varied with the structural damage severity. Despite the impedance variation, the structural damage did not modify the curve pattern of the imaginary EMI signatures, as revealed in Fig. 24(b). Further, the two impedance peaks shifted left according to the damage severity, indicating the reduction in the modal stiffness of the splice plate, see Fig. 24(a).

The changes in the peak frequencies and the peak magnitudes were quantified. Fig. 25(a) shows that Peak 1 experienced slight magnitude changes under the effect of the structural damage while that of Peak 2 was nearly unchanged (max variations: 19.98 Ω for Peak 1 and 0.66 Ω for Peak 2). As seen in Fig. 25(b), the two peak frequencies were slightly reduced with the same amount (max variations: 0.45 kHz for Peak 1 and Peak 2) when the splice plate was damaged.

5. Diagnosis of degraded smart interface using EMI responses and deep learning algorithm

5.1 CNN-based functional assessment method

A CNN-based method is proposed for assessing the health status of the smart interface during SHM, as shown in Fig. 26. The EMI features can be automatically extracted from the raw signal using a set of convolutional layers, and classified into one of four following classes: ‘Healthy’, ‘PZT-bond defect’, ‘PZT-breakage’, ‘Interface-debonding’ using a set of fully connected (fc) layers.

From the previous analyses, it is found that the degradations in the smart interface would cause three distinguishable patterns of imaginary impedance changes. They include upward shifts in the imaginary part induced by the degraded bonding layer of the sensor (e.g., shear lag and sensor debonding), downward shifts in the imaginary part caused by the degraded quality of the sensor (e.g., sensor breakage), and no shifts in the pattern of the imaginary part resulting from the interface detaching or the host structure’s damage. Therefore, the imaginary part is selected as the input for the CNN-based functional assessment model.

As shown in Fig. 26, the architecture of the CNN model is sequentially designed with (1) the input layer, (2) the convolutional (Conv) layer with 8 kernels of 1 × 128 (strike = 1), (3) the batch normalization (Batchnorm) layer of 8 channels, (4) the rectified linear unit (ReLU) layer, (5) the maxpooling (Maxpool) layer with a kernel of 1 × 4 (strike = 2), (6) the conv layer with 32 kernels of 1 × 8 (strike = 1), (7) the batchnorm layer of 32 channels, (8) the ReLU layer, (9) the fully connected (Fc) layer of 128, (10) the Fc layer of 64, (11) the Fc layer of 4 (i.e., the number of classes), (12) the Softmax layer, and (13) the class output layer. The

Table 1 The details of the operators of the CNN layers

No	Type	Depth	Filter	Stride
1	Input	-	-	-
2	Conv	8	1×128	1
4	Batchnorm	-	-	-
5	ReLU	-	-	-
2	Maxpool	8	1×4	2
6	Conv	32	1×8	1
7	Batchnorm	-	-	-
8	ReLU	-	-	-
9	Fc	128	-	-
10	Fc	64	-	-
11	Fc	4	-	-
12	Softmax	-	-	-
13	Output	-	-	-

specifications of the operators of those layers are summarized in Table 1.

The input layer is a 1-D imaginary EMI signal with a fixed size of 901 × 1 (901 is the number of swept frequencies). The Conv layer has convolutional kernels with weights to learn certain features of the input. The ReLU layer maps the negative values of the result of the previous layer to zero and keeps positive values. The ReLU layer helps to minimize the cost of computation and makes the process of training more efficient. The Batchnorm layer normalizes each channel of the input data across a mini-batch that help to speed up the process of training and reduce the sensitivity to the initialization of the network. The Maxpool layer slides the kernel on the output of the previous layer with a strike and for each position, only the maximum value is output. The Fc layer connects to all nodes of the previous layer and performs the dot product on the input data in each of the nodes. The Softmax layer takes the output of the Fc layer as the input data and applies the

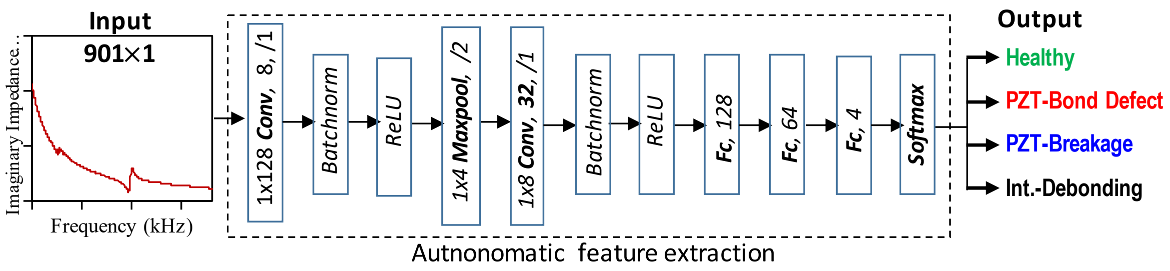

Fig. 26 The CNN-based functional assessment approach for smart interface

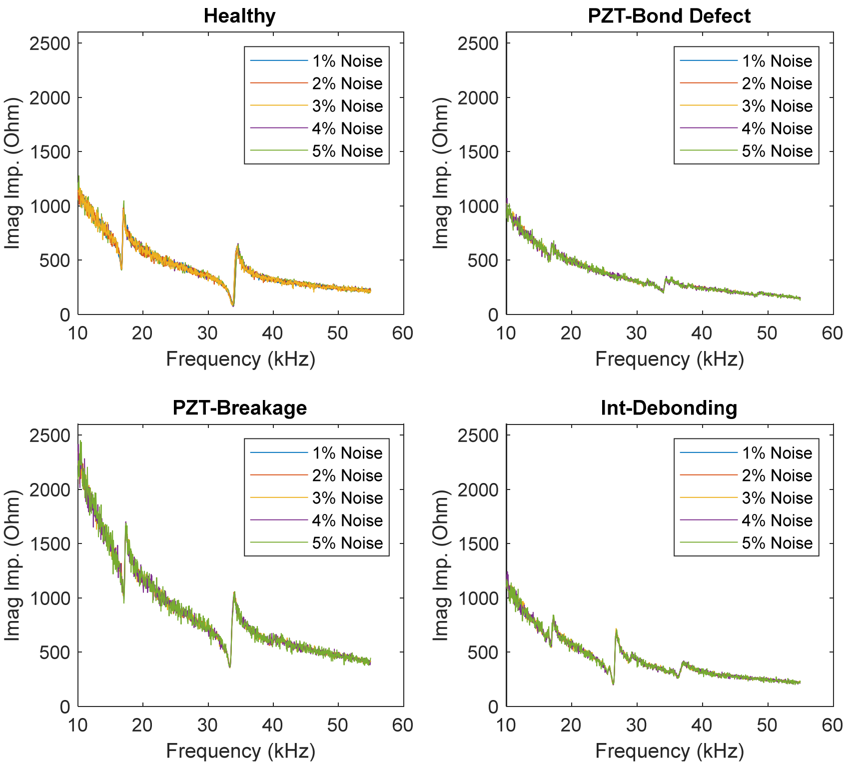

Fig. 27 Sample noise-contaminated signals for testing

softmax function. The details of these layers can be found in existing publications (LeCun *et al*. 1989, 2015, Gu *et al*. 2015).

5.2 Databank preparation and training the CNN

Two datasets were constructed for training and testing the CNN model. The imaginary EMI signals obtained from the previous simulations with some additional cases were used to build the training dataset. The additional cases include the vertical PZT debonding of 30%, the horizontal PZT debonding of 30%, the combined vertical and horizontal PZT debonding of 51%, the vertical PZT breakage of 30%, the horizontal PZT breakage of 30%, the combined vertical and horizontal PZT breakage of 51%, the vertical interface debonding of 69%, the horizontal interface debonding of 60%, the combined vertical and horizontal interface debonding of 87%, and the contact stiffness reductions of 20%, 40%, and 60%.

Briefly, the training dataset is composed of 42 imaginary EMI signals in which 7 signals (16.7%) for the "Healthy" class, 9 signals (21.4%) for the "Int.-debonding" class, 9

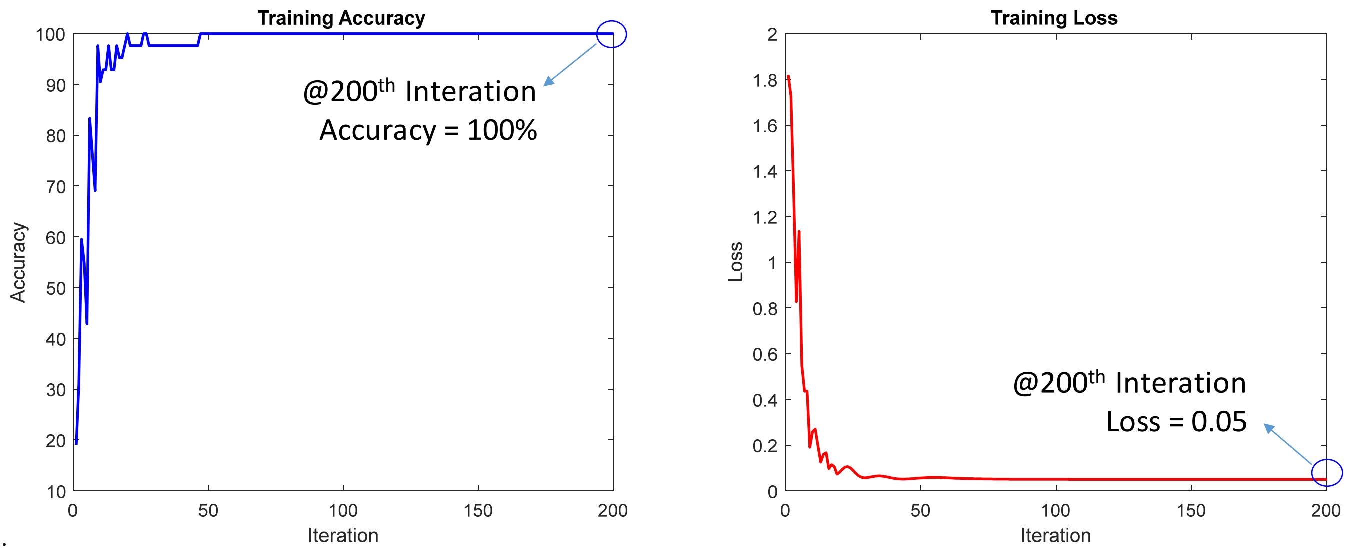

Fig. 28 Training the CNN model

Output Class \ Target Class	Healthy	Int-Debonding	PZT-Breakage	PZT-Debonding	
Healthy	**35** 16.7%	**0** 0.0%	**0** 0.0%	**2** 1.0%	94.6% 5.4%
Int-Debonding	**0** 0.0%	**45** 21.4%	**0** 0.0%	**0** 0.0%	100% 0.0%
PZT-Breakage	**0** 0.0%	**0** 0.0%	**45** 21.4%	**0** 0.0%	100% 0.0%
PZT-Debonding	**0** 0.0%	**0** 0.0%	**0** 0.0%	**83** 39.5%	100% 0.0%
	100% 0.0%	100% 0.0%	100% 0.0%	97.6% 2.4%	**99.0%** **1.0%**

Fig. 29 The accuracy of the CNN-based functional assessment method

signals (21.4%) for the “PZT-breakage” class, and 17 signals (40.5%) for “PZT-bond defect” class. It should be noted that the “Healthy” class includes the signals of both the intact case of the smart interface and the damage cases of the host structure (i.e., Young’s modulus and contact stiffness reductions). The “PZT-bond defect” class includes the signals of both the shear-lag cases and the PZT debonding cases.

To construct the testing dataset, the training signals were added by white noises with different levels of 1%, 2%, 3%, 4%, and 5% (i.e., the standard deviation of the signal amplitude), respectively. The addition of noises to the original signals is to consider the uncertainty in the EMI measurement encountered in realistic situations. Briefly, the testing dataset is composed of 210 signals in which 35 signals (16.7%) for the “Healthy” class, 45 signals (21.4%) for the “Int-debonding” class, 45 signals (21.4%) for the “PZT-breakage” class, and 85 signals (40.5%) for “PZT-bond defect” class. Fig. 27 shows the sample signals of the testing dataset. It is shown that the added noises caused certain changes in the imaginary EMI signals.

5.3 Evaluation of the CNN-based method for functional assessment in the smart interface

All experiments in this study were performed on a desktop computer (CPU: Intel Core i7-8700 of 3.2 GHz, memory: DDR4 of 16 GB, GPU: GeForce GT 1030 of 2 GB). The CNN model was programmed using Matlab language. The CNN was trained using the SGDM (stochastic gradient descent with momentum) training algorithm (the mini-batch size of 64, the momentum of 0.9, the learning rate of 0.001, the learning rate drop factor of 0.1).

The training accuracy and the training loss over the observations during the training process are plotted in Fig. 28. After 200 iterations, the overall accuracy of the CNN model reached 100% while the loss was significantly reduced to an ignorable value of 0.05, suggesting the high accuracy of the trained CNN model.

The performance of the CNN model was evaluated on the testing dataset. The classification result is illustrated using a fusion matrix chart, as shown in Fig. 29. The rows of the chart are the output classes (the predicted class) and the columns are corresponding to the target class (the true class). The diagonal cells are observations that are accurately classified. The off-diagonal cells are corresponding to observations that are incorrectly classified. In each cell, both the number of observations and the percentage of the total number of observations are shown. The far-right column on the chart shows the precision (positive predictive value) in green color and false discovery rate in red color for each class. The bottom row on the chart shows the recall (or true positive rate, in green color) and false negative rate (in red color) for each class. The bottom right cell of the chart corresponds to the overall accuracy.

Fig. 29 reveals a high level of consistency between the predicted classes and the true classes. The obtained results show that the proposed CNN-based method successfully predicted the health status of the smart interface, even with the noise-contaminated signals. The overall accuracy of the CNN model was as high as 99%.

6. Conclusions

In this study, a CNN-based method was developed for assessing the functionality of the smart interface during SHM. The method can autonomously extract and directly learn optimal EMI features from the raw signals. A predictive FE modelling strategy was adopted to establish a reliable FE model, from which the influences of the shear lag, sensor debonding, sensor breakage, interface detaching, and structural damage were extensively analyzed. The FE model was then used to generate a reliable EMI databank for training and testing the CNN. From the numerical and experimental investigations, at least four concluding remarks can be drawn, as follows:

1. The effect of the smart interface’s degradations on the EMI response was analytically realized using a refined impedance model.
2. The imaginary EMI signals showed distinctive changes under different functional degradations of the smart interface.
3. The proposed CNN-based method was successful to classify four types of the health status of the smart interface, including “Healthy”, “PZT-bond defect”, “PZT-breakage”, “Interface-debonding”.
4. The proposed method can directly process the raw EMI signal without preprocessing and is therefore promising for real-time assessment of the functionality of the smart interface in practice.

Despite those promising results, some limitations of this study remain unsolved. Firstly, the proposed CNN-based method was only verified on a bolted joint; the applicability of the method to more complex structures should be tested. Secondly, the proposed method is specifically designed for diagnosing single functional degradations; the method should be improved to assess combined degradation types.

Acknowledgments

This research is funded by Vietnam National Foundation for Science and Technology Development (NAFOSTED) under grant number 107.01-2019.332.

References

Abdeljaber, O., Avci, O., Kiranyaz, M.S., Boashash, B., Sodano, H. and Inman, D.J. (2018), “1-D CNNs for structural damage detection: Verification on a structural health monitoring benchmark data”, *Neurocomputing*, **275**, 1308-1317. https://doi.org/10.1016/j.neucom.2017.09.069

Ai, D., Luo, H. and Zhu, H. (2016), “Diagnosis and validation of damaged piezoelectric sensor in electromechanical impedance technique”, *J. Intell. Mater. Syst. Struct.*, **28**(7), 837-850. https://doi.org/10.1177/1045389x16657427

Annamdas, V.G.M., Radhika, M.A. and Yang, Y. (2009), "Easy installation method of piezoelectric (PZT) transducers for health monitoring of structures using electro-mechanical impedance technique", *Proceedings of Sensors and Smart Structures Technologies for Civil, Mechanical, and Aerospace Systems*, (Volume 7292, pp. 729227-729221), San Diego, CA, USA, March.

Azimi, M. and Pekcan, G. (2020), "Structural health monitoring using extremely compressed data through deep learning", *Comput.-Aided Civil Infrastr. Eng.*, **35**(6), 597-614. https://doi.org/10.1111/mice.12517

Bhalla, S. and Moharana, S. (2012), "A refined shear lag model for adhesively bonded piezo-impedance transducers", *J. Intell. Mater. Syst. Struct.*, **24**(1), 33-48. https://doi.org/10.1177/1045389x12457837

Dang, N.-L., Huynh, T.-C. and Kim, J.-T. (2019), "Local strand-breakage detection in multi-strand anchorage system using an impedance-based stress monitoring method—Feasibility study", *Sensors*, **19**(5), 1054. https://doi.org/10.3390/s19051054

Giurgiutiu, V., Zagrai, A. and Jing Bao, J. (2002), "Piezoelectric wafer embedded active sensors for aging aircraft structural health monitoring", *Struct. Health Monitor.*, **1**(1), 41-61. https://doi.org/10.1177/147592170200100104

Gresil, M., Yu, L., Giurgiutiu, V. and Sutton, M. (2012), "Predictive modeling of electromechanical impedance spectroscopy for composite materials", *Struct. Health Monitor.*, **11**(6), 671-683. https://doi.org/10.1177/1475921712451954

Gu, J., Wang, Z., Kuen, J., Ma, L., Shahroudy, A., Shuai, B., Liu, T., Wang, X., Wang, L. and Wang, G. (2015), "Recent advances in convolutional neural networks", *Pattern Recogn.*, **77**, 354-377. https://doi.org/10.1016/j.patcog.2017.10.013

Huynh, T.-C. (2020), "Structural parameter identification of a bolted connection embedded with a piezoelectric interface", *Vietnam J. Mech.*, 1-16. https://doi.org/10.15625/0866-7136/14806

Huynh, T.-C. (2021), "Vision-based autonomous bolt-looseness detection method for splice connections: Design, lab-scale evaluation, and field application", *Automat. Constr.*, **124**, 103591. https://doi.org/10.1016/j.autcon.2021.103591

Huynh, T.-C. and Kim, J.-T. (2014), "Impedance-based cable force monitoring in tendon-anchorage using portable PZT-interface technique", *Mathe. Problems Eng.*, **11**, Article 784731. https://doi.org/10.1155/2014/784731

Huynh, T.-C. and Kim, J.-T. (2017), "Quantitative damage identification in tendon anchorage via PZT interface-based impedance monitoring technique", *Smart Struct. Syst.*, *Int. J.*, **20**(2), 181-195. https://doi.org/10.12989/sss.2017.20.2.181

Huynh, T.C., Dang, N.L. and Kim, J.T. (2018), "Preload monitoring in bolted connection using piezoelectric-based smart interface", *Sensors*, **18**(9), 2766. https://doi.org/10.3390/s18092766

Huynh, T.-C., Lee, S.-Y., Dang, N.-L. and Kim, J.-T. (2019), "Sensing region characteristics of smart piezoelectric interface for damage monitoring in plate-like structures", *Sensors*, **19**(6), 1377. https://doi.org/10.3390/s19061377

Huynh, T.-C., Nguyen, T.-D., Ho, D.-D., Dang, N.-L. and Kim, J.-T. (2020), "Sensor Fault Diagnosis for Impedance Monitoring Using a Piezoelectric-Based Smart Interface Technique", *Sensors*, **20**(2), 510. https://doi.org/10.3390/s20020510

Jin, C. and Wang, X. (2011), "Analytical modelling of the electromechanical behaviour of surface-bonded piezoelectric actuators including the adhesive layer", *Eng. Fract. Mech.*, **78**(13), 2547-2562. https://doi.org/10.1016/j.engfracmech.2011.06.014

Johnson, K.L. (1985), *Contact Mechanics*, Cambridge University Press. https://doi.org/DOI: 10.1017/CBO9781139171731

Kim, J.-T., Park, J.-H., Hong, D.-S. and Park, W.-S. (2010), "Hybrid health monitoring of prestressed concrete girder bridges by sequential vibration-impedance approaches", *Eng. Struct.*, **32**(1), 115-128. https://doi.org/https://doi.org/10.1016/j.engstruct.2009.08.021

Kim, H., Liu, X., Ahn, E., Shin, M., Shin, S.W. and Sim, S.-H. (2019), "Performance assessment method for crack repair in concrete using PZT-based electromechanical impedance technique", *NDT & E Int.*, **104**, 90-97. https://doi.org/10.1016/j.ndteint.2019.04.004

LeCun, Y., Boser, B., Denker, J.S., Henderson, D., Howard, R.E., Hubbard, W. and Jackel, L.D. (1989), "Backpropagation applied to handwritten zip code recognition", *Neural Computat.*, **1**(4), 541-551. https://doi.org/10.1162/neco.1989.1.4.541

LeCun, Y., Bengio, Y. and Hinton, G. (2015), "Deep learning", *Nature*, **521**(7553), 436-444. https://doi.org/10.1038/nature14539

Li, W., Liu, T., Zou, D., Wang, J. and Yi, T.-H. (2019), "PZT based smart corrosion coupon using electromechanical impedance", *Mech. Syst. Signal Process.*, **129**, 455-469. https://doi.org/https://doi.org/10.1016/j.ymssp.2019.04.049

Liang, C., Sun, F.P. and Rogers, C.A. (1994), "Coupled electro-mechanical analysis of adaptive material systems-determination of the actuator power consumption and system energy transfer", *J. Intell. Mater. Syst. Struct*, **5**(1), 12-20. https://doi.org/10.1177/1045389x9400500102

Mansoor, M.B., Köble, S., Wong, T.W., Woias, P. and Goldschmidtböing, F. (2017), "Design, characterization and sensitivity analysis of a piezoelectric ceramic/metal composite transducer", *Micromachines*, **8**(9), 271. https://www.mdpi.com/2072-666X/8/9/271

Min, J., Park, S. and Yun, C.-B. (2010), "Impedance-based structural health monitoring using neural networks for autonomous frequency range selection", *Smart Mater. Struct.*, **19**(12), 125011. http://stacks.iop.org/0964-1726/19/i=12/a=125011

Nguyen, K.-D. and Kim, J.-T. (2012), "Smart PZT-interface for wireless impedance-based prestress-loss monitoring in tendon-anchorage connection", *Smart Struct. Syst.*, *Int. J.*, **9**(6), 489-504. https://doi.org/10.12989/sss.2012.9.6.489

Nguyen, K.-D., Lee, S.-Y., Lee, P.-Y. and Kim, J.-T. (2011), "Wireless SHM for bolted connections via multiple PZT-interfaces and Imote2-platformed impedance sensor node", *Proceedings of the 6th International Workshop on Advanced Smart Materials and Smart Structures Technology* (*ANCRiSST2011*), Dalian, China, July.

Ong, C., Yang, Y., Wong, Y., Bhalla, S., Lu, Y. and Soh, C.K. (2003), "Effects of adhesive on the electromechanical response of a piezoceramic-transducer-coupled smart system", In: *Smart Materials*, *Structures*, *and Systems*, Vol. 5062, pp. 241-247.

Park, G., Cudney, H.H. and Inman, D.J. (2001), "Feasibility of using impedance-based damage assessment for pipeline structures", *Earthq. Eng. Struct. Dyn.*, **30**(10), 1463-1474. https://doi.org/10.1002/eqe.72

Park, G., Farrar, C.R., Rutherford, A.C. and Robertson, A.N. (2006), "Piezoelectric active sensor self-diagnostics using electrical admittance measurements", *J. Vib. Acoust.*, **128**(4), 469-478. https://doi.org/10.1115/1.2202157

Park, S., Park, G., Yun, C.-B. and Farrar, C.R. (2008), "Sensor self-diagnosis using a modified impedance model for active sensing-based structural health monitoring", *Struct. Health Monitor.*, **8**(1), 71-82. https://doi.org/10.1177/1475921708094792

Pasquier, R. and Smith, I.F.C. (2016), "Iterative structural identification framework for evaluation of existing structures", *Eng. Struct.*, **106**, 179-194. https://doi.org/https://doi.org/10.1016/j.engstruct.2015.09.039

Ritdumrongkul, S., Abe, M., Fujino, Y. and Miyashita, T. (2004), "Quantitative health monitoring of bolted joints using a piezoceramic actuator–sensor", *Smart Mater. Struct.*, **13**(1), 20. http://stacks.iop.org/0964-1726/13/i=1/a=003

Ryu, J.-Y., Huynh, T.-C. and Kim, J.-T. (2019), "Tension force estimation in axially loaded members using wearable piezoelectric interface technique", *Sensors*, **19**(1), 47. https://doi.org/10.3390/s19010047

Shih, H.W., Thambiratnam, D.P. and Chan, T.H.T. (2009), "Vibration based structural damage detection in flexural members using multi-criteria approach", *J. Sound Vib.*, **323**(3), 645-661. https://doi.org/https://doi.org/10.1016/j.jsv.2009.01.019

Sirca, G.F. and Adeli, H. (2012), "System identification in structural engineering", *Scientia Iranica*, **19**(6), 1355-1364. https://doi.org/https://doi.org/10.1016/j.scient.2012.09.002

Song, G., Gu, H. and Mo, Y.-L. (2008), "Smart aggregates: multi-functional sensors for concrete structures—a tutorial and a review", *Smart Mater. Struct.*, **17**(3), 033001. https://doi.org/10.1088/0964-1726/17/3/033001

Stubbs, N. and Kim, J.T. (1996), "Damage localization in structures without baseline modal parameters", *AIAA J.*, **34**(8), 1644-1649. https://doi.org/10.2514/3.13284

Tawie, R., Park, H.B., Baek, J. and Na, W.S. (2019), "Damage detection performance of the electromechanical impedance (EMI) technique with various attachment methods on glass fibre composite plates", *Sensors*, **19**(5), 1000. https://www.mdpi.com/1424-8220/19/5/1000

Uddin, M.N., Islam, M.S., Sampe, J., Ali, S.H.M. and Bhuyan, M.S. (2016), "Design and simulation of piezoelectric cantilever beam based on mechanical vibration for energy harvesting application", *Proceedings of 2016 International Conference on Innovations in Science, Engineering and Technology* (*ICISET*), Dhaka, Bangladesh, October.

Xu, Y. and Liu, G. (2002), "A modified electro-mechanical impedance model of piezoelectric actuator-sensors for debonding detection of composite patches", *J. Intell. Mater. Syst. Struct.*, **13**(6), 389-396. https://doi.org/10.1177/104538902761696733

Yan, S., Sun, W., Song, G., Gu, H., Huo, L.-S., Liu, B. and Zhang, Y.-G. (2009), "Health monitoring of reinforced concrete shear walls using smart aggregates", *Smart Mater. Struct.*, **18**(4), 047001. https://doi.org/10.1088/0964-1726/18/4/047001

HJ